


**Measurement of irreversibility and entropy production via the tubular ensemble**Julian Kappler<sup>1</sup>\* and Ronojoy Adhikari*Department of Applied Mathematics and Theoretical Physics, Centre for Mathematical Sciences, University of Cambridge, Wilberforce Road, Cambridge CB3 0WA, United Kingdom* (Received 26 May 2021; accepted 2 February 2022; published 5 April 2022)

The appealing theoretical measure of irreversibility in a stochastic process, as the ratio of the probabilities of a trajectory and its time reversal, cannot be accessed directly in experiments since the probability of a single trajectory is zero. We regularize this definition by considering, instead, the limiting ratio of probabilities for trajectories to remain in the tubular neighborhood of a smooth path and its time reversal. The resulting pathwise medium entropy production agrees with the formal expression from stochastic thermodynamics and can be obtained from measurable tube probabilities. Estimating the latter from numerically sampled trajectories for Langevin dynamics yields excellent agreement with theory. By combining our measurement of pathwise entropy production with a Markov chain Monte Carlo algorithm, we infer the entropy-production distribution for a transition path ensemble directly from short recorded trajectories. Our work enables the measurement of irreversibility along individual paths and path ensembles in a model-free manner.

DOI: [10.1103/PhysRevE.105.044107](https://doi.org/10.1103/PhysRevE.105.044107)**I. INTRODUCTION**

Stochastic processes without memory have been used to describe the dynamics of physical systems starting with the pioneering work of Rayleigh, Einstein, and Smoluchowski [1]. The phenomenological observation that systems out of equilibrium display irreversibility has prompted a search for theoretical measures that enable its quantification. The first of these measures was provided by Kolmogorov [2,3] by considering the joint distribution of pairs of points along a stochastic trajectory and its time reversal. This characterization was refined by Ikeda and Watanabe [4] by considering the probabilities for stochastic trajectories to remain in the tubular neighborhood of a smooth path and its time reversal. This line of thought reached its culmination in the elementary definition of irreversibility as the ratio of probabilities for a trajectory and its reverse in the work of Maes and Netočný [5] and Seifert [6]. The latter provides the clearest derivation of the plethora of results known as fluctuation theorems [7–13], yields a definition of the medium entropy production as the logarithm of the ratio of the probability of forward and backward paths [6], and has engendered the thriving field of stochastic thermodynamics [13–15].

Despite the theoretical importance of the elementary definition of irreversibility, measurements, in both experiment and simulation, have focused on ensembles of trajectories [16–19] or systems with discrete state space [20], and the medium entropy production along a single continuous trajectory has not yet been measured directly. This is because the probability of a trajectory (and of its reversal) is, strictly speaking, zero, and it is therefore not obvious how to infer the ratio of probabilities for a pair of forward and reverse paths. Hence,

while theoretical expressions for this ratio can be evaluated on observed trajectories, the result cannot be tested without an independent, model-free method of inferring pathwise irreversibility.

In this work, we provide a resolution to this impasse by considering, instead of a single trajectory, the probability of an ensemble of trajectories to remain within the tubular neighborhood of a smooth path [21,22]. We define the logarithm of the probability ratio for forward and backward tubes, as the tube radius goes to zero, as a measure of irreversibility. We show that this coincides with the stochastic thermodynamic expression for the medium entropy production when the latter is restricted to smooth paths. Since the probability to remain within a finite-radius tube can be measured directly [22], we obtain the medium entropy production by extrapolating ratios of measured finite-radius tube probabilities to the limit of vanishing radius. This requires no knowledge of the underlying process (other than that it is memoryless), and our method, then, yields a model-free route to obtaining the entropy production along individual paths. This establishes a protocol for directly measuring irreversibility along individual pathways and allows us to investigate this phenomenon, experimentally or numerically, in a manner that is more refined than full ensemble averages. We validate our method in an explicit numerical example. For two-dimensional Langevin dynamics with a nonequilibrium force, we directly infer the medium entropy production along individual paths from simulated trajectories without using any knowledge about the underlying dynamics beyond Markovianity and we find excellent agreement with the theoretical expectation [6]. Furthermore, by combining the direct measurements of relative path probabilities [22], our approach to the single-trajectory entropy production, and a Metropolis-Hastings Markov chain Monte Carlo (MCMC) algorithm [23], we infer the distribution of the entropy production for

\*jkappler@posteo.de

a transition path ensemble directly from measured sojourn probabilities.

The remainder of this paper is organized as follows. In Sec. II we define the medium entropy production as the limiting ratio of tube probabilities and discuss analytically the special case for overdamped Itô-Langevin dynamics. We subsequently explain how we infer finite-radius tube probabilities from recorded time series in practice [22]. In Sec. III we then consider a two-dimensional example system. Using a data set generated via numerical simulations, we first measure the entropy production along individual paths and compare the results to analytical predictions. We then go on to infer the entropy production distribution for a transition path ensemble, using only measured tube probabilities, and compare the results to an independently generated transition path ensemble based on direct Langevin simulations. We analyze these transition path ensembles further, by considering both paths with very small entropy production and paths with very large entropy production. In Sec. IV we close by summarizing our results and discussing further implications.

## II. IRREVERSIBILITY VIA ASYMPTOTIC TUBE PROBABILITIES

### A. Entropy production as asymptotic ratio of tube probabilities

For a smooth reference path  $\varphi$ ,  $t \in [0, t_f]$ , we define the sojourn probability that a stochastic trajectory  $\mathbf{x}_t$  remains within a tube of radius  $R$  around  $\varphi$  as  $P_R^\varphi(t) \equiv P(\|\mathbf{x}_s - \varphi_s\| < R \forall s \in [0, t])$ , where  $\|\mathbf{v}\| = (v_1^2 + v_2^2 + \dots + v_N^2)^{1/2}$  denotes the standard Euclidean norm in  $\mathbb{R}^N$ , and where we suppress the dependence on the initial condition of the trajectory inside the tube [21]. Combining the approach to irreversibility via tubes [4] with the single-trajectory medium entropy production [6,13], we define the medium entropy change along  $\varphi$  in terms of asymptotic tube probabilities as

$$\Delta s_m[\varphi] \equiv \lim_{R \rightarrow 0} \ln \frac{P_R^\varphi(t_f)}{P_R^{\tilde{\varphi}}(t_f)}, \quad (1)$$

with  $\tilde{\varphi}_t \equiv \varphi_{t_f-t}$  the time reversal of the path  $\varphi$ . In our definition Eq. (1) we assume that temperature  $T$  is measured in units of energy, so that entropy is dimensionless [24]. Equation (1) relates the medium entropy production along a single path to observable sojourn probabilities. For finite radius  $R$ , the ratio of sojourn probabilities for forward and backwards paths can be measured without fitting a model to the data by simply counting how many sample trajectories leave the tube along forward and backward paths, respectively [21,22]. According to Eq. (1), performing this measurement for several finite values of  $R$ , and extrapolating the resulting log ratios to  $R \rightarrow 0$ , the medium entropy production  $\Delta s_m$  is obtained.

The decay of the sojourn probability is described by  $\alpha_R^\varphi(t)$ , the instantaneous exit rate with which stochastic trajectories first leave the tube, as [21]

$$\alpha_R^\varphi(t) \equiv -\frac{(\partial_t P_R^\varphi)(t)}{P_R^\varphi(t)}. \quad (2)$$

Differentiating Eq. (1) with respect to  $t_f$ , substituting  $t_f$  with  $t$ , and eliminating sojourn probabilities in favor of exit rates,

we obtain

$$\frac{d}{dt} \Delta s_m[\varphi] = -\lim_{R \rightarrow 0} \Delta \alpha_R^\varphi(t), \quad (3)$$

where

$$\Delta \alpha_R^\varphi(t) \equiv \alpha_R^\varphi(t) - \alpha_R^{\tilde{\varphi}}(t_f - t). \quad (4)$$

Equation (3) relates the change in medium entropy production along a single path to the difference of instantaneous tubular exit rates around forward and backward versions of the path.

### B. Analytical results for Langevin dynamics

While Eqs. (1)–(4) do not assume a model for the stochastic evolution of  $\mathbf{x}_t$ , for a given model the exit rate can be calculated analytically. We now consider the overdamped Itô-Langevin equation for an  $N$ -dimensional coordinate  $\mathbf{x}_t \equiv (x_1(t), x_2(t), \dots, x_N(t))$ , given by

$$d\mathbf{x}_t = \mu \mathbf{F}(\mathbf{x}_t) dt + \sqrt{2\mu T} d\mathbf{W}_t, \quad (5)$$

where  $\mu = D/T$  is the mobility with  $D$  the diffusion coefficient and  $T$  the absolute temperature measured in units of energy,  $\mathbf{F}$  is a deterministic force, and  $d\mathbf{W}_t$  denotes the increment of the Wiener process. While we here consider only forces that do not depend on time explicitly, our approach remains valid for time-dependent forces as long as for time-reversed paths the explicit time dependence of the force is also reversed [13]. For Eq. (5), the leading-order expansion of  $\alpha_R^\varphi(t)$  in the tube radius  $R$  is [21,25,26]

$$\alpha_R^\varphi(t) = \frac{C_N}{R^2} + \mathcal{L}^\varphi(t) + O(R^2), \quad (6)$$

where  $C_N$  is a constant which depends on only the dimension  $N$ , and the Onsager-Machlup (OM) Lagrangian  $\mathcal{L}^\varphi$  is given by [21,25–29]

$$\mathcal{L}^\varphi = \frac{1}{4D} [\dot{\varphi} - \mu \mathbf{F}(\varphi)]^2 + \frac{1}{2} \text{div}[\mu \mathbf{F}(\varphi)]. \quad (7)$$

Substituting Eq. (7) into the difference of exit rates Eq. (4) for forward and reverse paths, the relation

$$\lim_{R \rightarrow 0} \Delta \alpha_R^\varphi(t) = -\frac{1}{T} \mathbf{F}(\varphi_t) \cdot \dot{\varphi}_t \quad (8)$$

between the limit of exit-rate difference and work rate along  $\varphi$  follows. In turn substituting this into Eq. (3), and integrating with respect to time, yields the familiar formula [6,13]

$$\Delta s_m[\varphi] = \frac{1}{T} \int_0^{t_f} \mathbf{F}(\varphi_t) \cdot \dot{\varphi}_t dt, \quad (9)$$

which relates the medium entropy production and the work performed along  $\varphi$ .

### C. Measuring the exit rate from sample trajectories

To infer the entropy production from finite-radius exit rates, the log ratio on the right-hand side of Eq. (1) needs to be measured for small but finite radius  $R$ . In practice it can be difficult to acquire sufficient data for this measurement, because the number of trajectories which remain inside the tube decreases exponentially with time  $t$ . To overcome this problem, we employ a cloning algorithm, which is illustrated

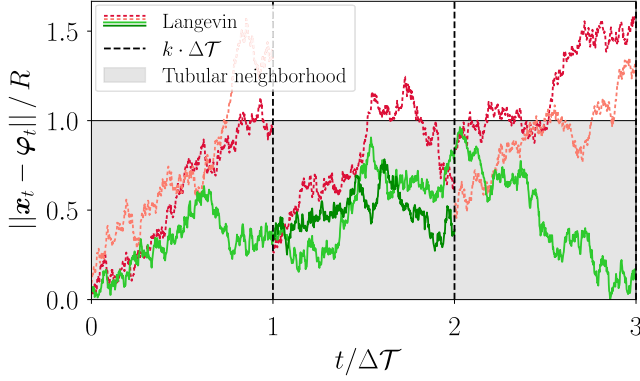


FIG. 1. The gray shaded area denotes a tube of radius  $R$  around a reference path  $\varphi$ . From a given set of short sample trajectories, we randomly draw  $M_0 = 3$  samples of duration  $\Delta\mathcal{T}$  (vertical dashed lines), all of which start close to  $\varphi_0$ . Trajectories which leave the tube (dotted red lines) are discarded, and the final positions of the trajectories that stay (solid green lines) are collected. We again draw  $M_1 = 3$  sample trajectories, with initial conditions approximately distributed as the previous final positions. We repeat the process of drawing sample trajectories and tracking whether or not they leave the tube, until we obtain the sojourn probability up to the desired final time. For each interval  $[l\Delta\mathcal{T}, (l+1)\Delta\mathcal{T}]$ , the sojourn probability is estimated as the fraction of trajectories that leave the tube during the time  $\Delta\mathcal{T}$ , divided by the initial number of trajectories  $M_l$ . We choose the small value  $M_l = 3$  here for illustration; to calculate exit rates from simulations we use values of the order  $10^5$ ; see Appendix B. For the data shown here we use the reference path  $\varphi \equiv \varphi^{(1)} = L(t/t_f, t/t_f)$  and the force (10) with  $\theta = 1$ ,  $LF_0/T = 5$ . Furthermore, we use  $R = 0.3L$ ,  $\Delta\mathcal{T} = 0.01\tau$ , and  $D = L^2/\tau$ .

in Fig. 1 and has previously been used to infer finite-radius exit rates from one-dimensional experimental time series [22]. We here present a short summary of the algorithm and give more details in Appendix B.

The cloning algorithm assumes that the underlying stochastic dynamics is Markovian, and that an ensemble of recorded short trajectories with initial conditions throughout the domain of interest are available; these can originate either from measurements [22] or, as in this work, from simulations.

For a given reference path  $\varphi$  and tube radius  $R$ , we initialize the algorithm by drawing from the ensemble of recorded trajectories a large number  $M_0$  of sample trajectories, with initial conditions close to  $\varphi_0$ . We then follow those sample trajectories for a short time  $\Delta\mathcal{T}$  and discard each trajectory once it leaves a moving ball of radius  $R$  and instantaneous center  $\varphi_t$  for the first time. We then estimate the sojourn probability  $P_R^\varphi(t)$  at time  $t \in [0, \Delta\mathcal{T}]$  by the fraction of sample trajectories that have never left the tube until the time  $t$ .

To iteratively obtain the sojourn probability also for any subsequent time interval  $[l\Delta\mathcal{T}, (l+1)\Delta\mathcal{T}]$ , we in each iteration step draw  $M_l$  sample trajectories with initial conditions inside a ball of radius  $R$  and with center  $\varphi(l\Delta\mathcal{T})$ . For the initial distribution within the ball, we at each iteration use the final spatial distribution of those trajectories that have never left the tube in the previous iteration. We repeat this iteration step until  $l\Delta\mathcal{T} = t_f$ .

By periodically drawing new samples after a short time  $\Delta\mathcal{T}$ , we overcome the exponential decay of the trajectories

that have never left the tube. For a given  $\Delta\mathcal{T}$ , we choose the number of trajectories  $M_l$  dynamically based on the expected decay of the sojourn probability during the time interval  $[l\Delta\mathcal{T}, (l+1)\Delta\mathcal{T}]$ , as we explain in detail in Appendix B. In practice, one wants to choose the time  $\Delta\mathcal{T}$  so as to balance the exponential decay of the sojourn probability with the cost of redrawing sample trajectories: If  $\Delta\mathcal{T}$  is too large, a large number of sample trajectories  $M_l$  is required to reliably estimate the sojourn probability for the whole time interval  $[l\Delta\mathcal{T}, (l+1)\Delta\mathcal{T}]$ . On the other hand, if  $\Delta\mathcal{T}$  is too small, new trajectory samples have to be drawn very frequently.

### III. TWO-DIMENSIONAL NONEQUILIBRIUM EXAMPLE

#### A. Model system

For a length scale  $L$  and a timescale  $\tau$ , we consider Eq. (5) for dimension  $N = 2$  with diffusivity  $D = L^2/\tau$ , so that  $\tau_D \equiv L^2/D = \tau$ . We consider a shear force

$$\mathbf{F}(\mathbf{x}) = \frac{\theta F_0}{L} \begin{pmatrix} x_2 \\ 0 \end{pmatrix}, \quad (10)$$

where we fix  $LF_0/T = 5$ , so that the dimensionless parameter  $\theta \in \mathbb{R}$  controls the force amplitude. Equation (10) does not admit a potential and is illustrated as a quiver plot in Fig. 2(a). For each of the values  $\theta = 0, 0.5, 1, 1.5, 2$ , we generate an independent set of short sample Langevin trajectories with random initial conditions, as described in detail in Appendix A.

#### B. Entropy production along individual paths

We consider a family of paths

$$\varphi_t^{(n)} = L \begin{pmatrix} t/t_f \\ (t/t_f)^n \end{pmatrix}, \quad (11)$$

where  $t \in [0, t_f] \equiv [0, \tau]$ , the length scale  $L$  multiplies both vector components, and  $n \in \mathbb{N}$  enumerates the paths. For any  $n$ , the path starts at  $\mathbf{x}_0 = (0, 0)$  and ends at  $\mathbf{x}_f = (L, L)$ . Example paths for  $n = 1$  and  $n = 4$  are shown in Fig. 2(a). For this family of paths and the force (10), the analytical medium entropy production (9) evaluates to

$$\Delta s_m[\varphi^{(n)}] = \frac{LF_0}{T(n+1)}\theta. \quad (12)$$

We now consider the case  $n = 1$ . We use the cloning algorithm described in Sec. IIC and Appendix B with  $\Delta\mathcal{T} = 0.01\tau_D$  to measure the finite-radius sojourn probability for both  $\varphi^{(1)}$  and its time reverse  $\tilde{\varphi}^{(1)}$  for radius  $R/L = 0.3, 0.4, 0.5, 0.6, 0.7$ . We fit a quadratic function  $f(R) = a + R^2b$  to the resulting measured log ratios  $\ln P_R^\varphi(t_f)/P_R^{\tilde{\varphi}}(t_f)$ , and extrapolate to zero as  $\lim_{R \rightarrow 0} \ln P_R^\varphi(t_f)/P_R^{\tilde{\varphi}}(t_f) = a$ , where here  $\varphi \equiv \varphi^{(1)}$ . The quadratic form of the fit function  $f(R)$  is motivated by Eq. (6), according to which no terms linear in  $R$  appear in the exit rate and hence in the log ratio of sojourn probabilities. In Fig. 2(b) the extrapolated measured log ratio is compared to the corresponding analytical expectation, given by the right-hand side of Eq. (12). We observe that the measurement agrees very well with the theoretical prediction, which shows that Eq. (1) can be used to infer the irreversibility along individual paths directly from data. This

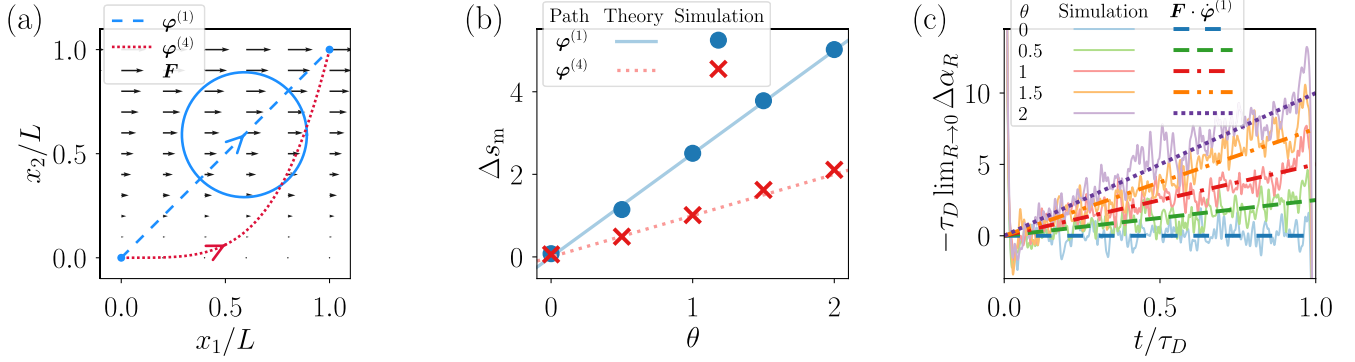


FIG. 2. (a) The shear force Eq. (10) is shown as black quiver plot. The path defined in Eq. (11) is shown for  $n = 1$  (dashed blue line) and  $n = 4$  (dotted red line), with arrows indicating the forward direction. For  $\varphi^{(1)}$  we include a snapshot of the instantaneous tube of radius  $R/L = 0.3$  around the path (blue circle). (b) The colored lines denote the theoretical entropy production, Eq. (12), as a function of  $\theta$  for  $n = 1$  (solid blue line) and  $n = 4$  (dotted red line). The colored symbols are obtained by extrapolating measured finite-radius log ratios of sojourn probabilities to  $R = 0$ , to evaluate Eq. (1). (c) The colored solid lines denote the negative of the left-hand side of Eq. (8), obtained by extrapolating measurements of Eq. (4), for the reference path  $\varphi^{(1)}$ , to  $R = 0$ . The colored broken lines denote the corresponding theoretical predictions given by the negative of the right-hand side of Eq. (8), calculated using the force Eq. (10) with  $LF_0/T = 5$ . Numerical data in (c) are smoothed using a Hann window of width  $0.015 \tau_D$ .

is further confirmed by repeating the analysis protocol for a second path, where  $n = 4$ . Figure 2(b) shows that also here the extrapolated log ratio obtained from direct measurement agrees very well with the theoretical prediction.

To see how the medium entropy production is partitioned along the path, we evaluate the instantaneous exit rate for forward and backward paths for the  $n = 1$  path. For this we discretize Eq. (2) using central finite differences and evaluate the expression on the measured sojourn probability for  $R/L = 0.3, 0.4, 0.5, 0.6, 0.7$ . To extrapolate the resulting finite-radius measurements of Eq. (4) to the limit  $R \rightarrow 0$ , we at each recorded time  $t$  fit a quadratic function  $f(t) = a(t) + R^2 b(t)$  to the measured exit-rate difference  $\Delta \alpha_R^\varphi(t)$ . From this fit, we obtain the extrapolated exit-rate difference at time  $t$  as  $\lim_{R \rightarrow 0} \Delta \alpha_R^\varphi(t) = a(t)$  [22]. In Fig. 2(c) we compare the resulting extrapolated exit-rate differences to the theoretical Eq. (8). While overall the agreement between measurement and theory is very good, there are deviations both in the beginning,  $t \lesssim 0.05 \tau_D$  and at the end of the trajectory,  $t \gtrsim 0.95 \tau_D$ . This is because in our cloning algorithm all initially sampled trajectories start close to the center of the tube, so that at the beginning (end) we observe the initial relaxation of this initial condition for the forward (reverse) path [21]. The agreement in Fig. 2(b) shows that these transient effects are not important for the integrated change in medium entropy production, i.e., for  $\Delta s_m$ .

In Appendix E we consider another two-dimensional example system, comprising a circular double-well potential superimposed with a circular nonequilibrium force; the example again confirms the validity and practical applicability of Eqs. (1) and (3).

### C. Medium entropy production for transition-path ensemble

We now infer the entropy-production distribution for an ensemble of transition paths, using only measured sojourn probabilities. For this, we use the data set of Langevin time series corresponding to the force (10), with  $LF_0/T = 5$ ,

$\theta = 1$ , and  $D = L^2/\tau$ . We consider continuous paths which start at  $\mathbf{x}_0 = (0, 0)$  at time  $t = 0$ , and end at  $\mathbf{x}_f = (L, L)$  at time  $t_f = \tau_D$ . We approximate the infinite-dimensional space of all such paths by a path space of dimension  $d = NM$ , where for our two-dimensional system  $N = 2$ . Our finite-dimensional approximation of path space is parametrized by a set of  $M$   $N$ -dimensional expansion coefficients  $\mathbf{a} \equiv (\mathbf{a}_1, \dots, \mathbf{a}_M) \in \mathbb{R}^{N \times M}$ . For any  $\mathbf{a}$ , the corresponding path is then given by

$$\varphi_t(\mathbf{a}) = \mathbf{x}_f \frac{t}{\tau_D} + \sum_{k=1}^M \frac{\mathbf{a}_k}{k} \sin\left(k\pi \frac{t}{\tau_D}\right). \quad (13)$$

We use  $M = 15$ , so that for our  $N = 2$  dimensional system we have  $d = 30$ , and run a Metropolis-Hastings Markov chain Monte Carlo (MCMC) algorithm [23] on the space  $\mathbb{R}^d$ , to infer the distribution of  $\Delta s_m$ ; we explain the algorithm in detail in Appendix C. Crucially, the algorithm uses only measured sojourn probabilities. First, to generate an ensemble of transition paths, ratios of path probabilities need to be evaluated; for this we use extrapolated log ratios of measured finite-radius sojourn probabilities [22]. Second, we obtain the medium entropy production along each path from measured finite-radius sojourn probabilities via Eq. (1). Using the sojourn-probability MCMC algorithm, we generate a set of  $57\,448 \approx 5.7 \times 10^4$  transition paths and accompanying values for  $\Delta s_m$ .

For comparison, we additionally generate an independent ensemble of transition paths. Using the Euler-Maruyama integration scheme with time step  $\Delta t/\tau_D = 10^{-4}$ , we run a large number of numerical simulations of Eq. (5), each of duration  $\tau_D$  and with initial condition  $\mathbf{x}_0 = (0, 0)$ . We retain only those trajectories that at the final time are within the rectangle  $[0.9L, 1.1L] \times [0.9L, 1.1L]$  around  $\mathbf{x}_f = (L, L)$ . Using this protocol, we create an ensemble of  $3\,316\,727 \approx 3.3 \times 10^6$  Langevin transition paths. For each trajectory, we evaluate Eq. (9) to obtain the corresponding analytical prediction for  $\Delta s_m$  [30].

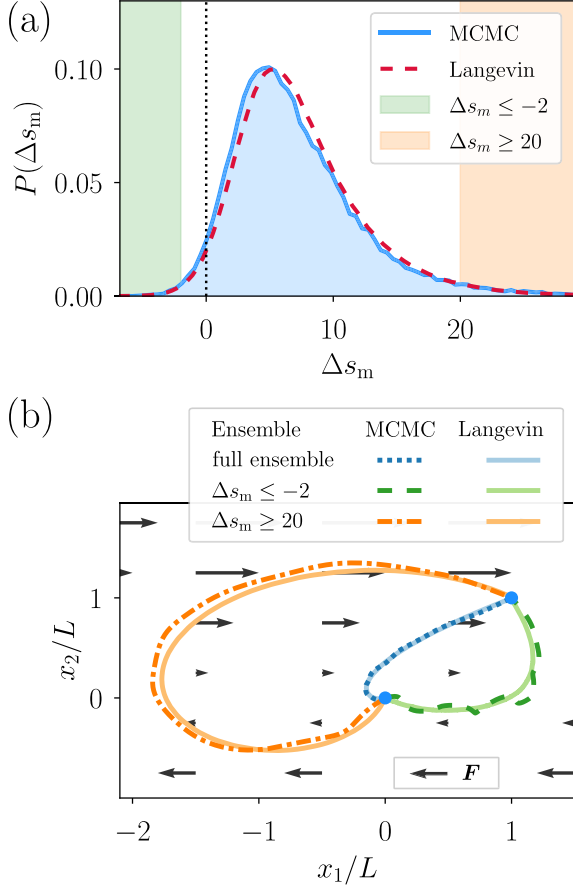


FIG. 3. (a) Distribution of  $\Delta s_m$  for the ensemble of transition paths that start at  $\mathbf{x}_0 = (0, 0)$  and are at  $\mathbf{x}_f = (L, L)$  a duration  $\tau_D$  later. The solid blue curve is obtained from approximately  $5.7 \times 10^4$  samples generated via an MCMC algorithm, which uses only measured sojourn probabilities. Full details on the algorithm are given in Appendix C. The dashed red line is obtained from evaluating Eq. (9) on an independently generated ensemble of transition paths, as explained in Sec. III C. The vertical dotted line denotes  $\Delta s_m = 0$ ; the colored shaded regions depict the ranges  $\Delta s_m < -2$  (green) and  $\Delta s_m \geq 20$  (orange). (b) The broken lines depict the mean transition paths inferred from the MCMC algorithm; the solid lines correspond to the mean transition paths obtained from direct Langevin simulations. While the dotted and solid blue lines correspond to the mean over the whole ensemble, the green and orange lines depict the mean over all sample paths with  $\Delta s_m \geq 20$  (dashed-dotted and solid orange lines) and  $\Delta s_m \leq -2$  (dashed and solid green lines). For all data shown, we fix a length scale  $L$  and a timescale  $\tau$  and consider the force (10), with  $\theta = 1$  and  $LF_0/T = 5$ , as well as  $D = L^2/\tau$ .

In Fig. 3(a) we show the resulting distribution for  $\Delta s_m$ , obtained from both the sojourn-probability MCMC and the direct Langevin simulations. Our MCMC algorithm, which uses only measured sojourn probabilities inferred from short recorded time series, reproduces the distribution of the medium entropy production for the ensemble very well; the slight deviations between the two data sets can be explained by our low-dimensional approximation Eq. (13) of path space, as we discuss in Appendix D.

Both the sojourn-probability MCMC and the direct Langevin simulations yield an ensemble of transition paths

with accompanying entropy production. We now analyze this ensemble further, to gain insight into the mean behavior of small- and large-entropy transition paths.

We first calculate the mean transition path from both ensembles by at each time  $t$  averaging over the current positions of all trajectories in the respective ensemble. In Fig. 3(b) we show the resulting mean transition paths as dotted and solid blue lines, which agree very well.

We next consider the subensemble of paths with small entropy production  $\Delta s_m \leq -2$ , as indicated by the green shaded region on the left side of Fig. 3(a). Out of our data set of 57 448 MCMC sample paths, 294 fulfill  $\Delta s_m \leq -2$ , so that we estimate the probability to observe any such small-entropy path as  $P(\Delta s_m \leq -2) \approx 294/57\,448 \approx 5.1 \times 10^{-3}$ . This is close to the corresponding value  $P(\Delta s_m \leq -2) \approx 15\,697/3\,316\,727 \approx 4.7 \times 10^{-3}$  estimated from the direct Langevin simulations. We calculate the mean small-entropy path by at any time  $t$  averaging over all the positions of all paths with  $\Delta s_m \leq -2$  and show the corresponding results in Fig. 3(b) as dashed and solid green curves. Again, the MCMC result agrees well with the mean small-entropy path obtained from direct Langevin simulations; we rationalize the oscillatory behavior of the MCMC path by the small number of samples. From Fig. 3(b) we observe that small-entropy paths on average move to  $x_1 \approx L$  with a very small negative value of  $x_2$  and move up to  $\mathbf{x}_f$  slightly against the shear force. This motion against the deterministic force is how these trajectories perform work, i.e., how they obtain a negative medium entropy production.

We finally consider paths with large medium entropy production  $\Delta s_m \geq 20$ , as indicated by the orange shaded region on the right side of Fig. 3(a). In our MCMC ensemble, there are 1335 MCMC sample paths with  $\Delta s_m \geq 20$ , so that we estimate  $P(\Delta s_m \geq 20) \approx 1335/57\,448 \approx 2.3 \times 10^{-2}$ , which compares well with the corresponding ratio  $P(\Delta s_m \geq 20) \approx 71\,588/3\,316\,727 \approx 2.2 \times 10^{-2}$  obtained from the direct Langevin simulations. Also for all paths with  $\Delta s_m \geq 20$ , we calculate the mean path from both the MCMC sample paths and the direct Langevin trajectories. We show the resulting mean paths in Fig. 3(b) as dash-dotted and solid orange curves and again observe good agreement. As the figure shows, paths that significantly dissipate energy into the heat bath move along the shear force  $F$  most of the time: The mean path first moves towards negative  $x_1$  values in the lower half-plane, and then moves towards  $\mathbf{x}_f$  in the upper half-plane.

Overall, Fig. 3 shows that the tubular-ensemble approach to the entropy production enables us to quantify and analyze the irreversibility of a path ensemble using only directly measured sojourn probabilities.

#### IV. DISCUSSION

We have shown that the pathwise medium entropy production can be obtained from the ratio of probabilities for trajectories to remain within a tube encircling a path in the limit of the tube radius going to zero. As we demonstrate, by analyzing ensembles of short simulated trajectories, the entropy production along an individual path can be inferred from data without any knowledge of the underlying dynamics other than assuming it to be memoryless. By combining this

measurement of irreversibility along individual paths with a Markov chain Monte Carlo (MCMC) algorithm, we obtain the irreversibility for path ensembles, using only measured sojourn probabilities. The path ensemble we generate via our MCMC algorithm allows us to probe the mean behavior of small- and large-entropy paths.

Our work shows clearly that by considering individual paths as limits of finite-radius tubes, which from an experimental point of view is a natural perspective, both single-trajectory and path-ensemble properties can be inferred from recorded time series without the need to parametrize a model. Our definition of the medium entropy production, Eq. (1), does not involve nondifferentiable stochastic trajectories and thus generalizes to processes with configuration-dependent diffusivities in a manner that sidesteps delicate issues of stochastic integration (i.e., the Itô-Stratonovic dilemma) [31–33]. The exit rate provides information beyond the entropy production, as Eq. (8), with the differential  $\dot{\varphi}_t dt$  chosen along  $N$  linearly independent directions, can be used to measure the drift  $\mathbf{F}$  of the process, without the need to estimate the diffusivity. Our work raises the question of how the medium entropy production could be generalized to tubes of finite radius and what the relationship of such a definition would be to the single-trajectory and full-ensemble measures of entropy production. Finally, our work suggests a generalization to stochastic field theories with broken detailed balance that are used to describe the fluctuating dynamics of active matter [34].

#### ACKNOWLEDGMENTS

Work was funded in part by the European Research Council under the EU’s Horizon 2020 Program, Grant No. 740269, and in part by the Royal Society through grant RP17002.

#### APPENDIX A: SAMPLE DATA PREPARATION

We fix a length scale  $L$  and a timescale  $\tau$ , and partition  $\mathbb{R}^2$  into a regular grid

$$S_{ij} \equiv [(i - 1/2)\Delta x, (i + 1/2)\Delta x] \times [(j - 1/2)\Delta y, (j + 1/2)\Delta y], \quad (\text{A1})$$

where  $i, j \in \mathbb{Z}$ . We use  $\Delta x = \Delta y = 0.05L$  and consider the range  $-100 \leq i \leq 90$ ,  $-60 \leq j \leq 70$ . The corresponding  $S_{ij}$  then cover the domain  $[-5.05L, 4.5L] \times [-3L, 3.5L] \subset \mathbb{R}^2$ , which is sufficient for our purposes, as we do not consider any tubes that extend outside this domain.

For each tuple  $(i, j)$ , we run 1500 independent simulations of the overdamped Itô-Langevin Eq. (5). Each trajectory starts in  $S_{ij}$ , and we draw the initial condition from a uniform distribution on  $S_{ij}$ . We then run the standard Euler-Maruyama algorithm for a duration  $\Delta\mathcal{T} = 0.01\tau$  using a time step  $\Delta t = 10^{-4}\tau$ . Every simulation thus consists of  $K = \Delta\mathcal{T}/\Delta t = 10^2$  time steps. We use the shear force (10) with  $LF_0/T = 5$  and diffusivity  $D = L^2/\tau$ . Using this protocol, we generate one independent data set for each value  $\theta = 0, 0.5, 1, 1.5, 2$  of the dimensionless parameter from Eq. (10).

#### APPENDIX B: CLONING ALGORITHM FOR INFERRING SOJOURN PROBABILITIES AND EXIT RATES FROM RECORDED TIME SERIES

We now explain how we extract finite-radius sojourn probabilities and their associated instantaneous exit rates from a set of time series, such as the one described in Appendix A. The algorithm described here is the two-dimensional generalization of a similar algorithm previously used on one-dimensional experimental time series [22] and is illustrated in Fig. 1. We assume as given a path  $\varphi$ , defined for time  $[0, t_f]$ , and a tube radius  $R$ , as well as a data set as described in Appendix A, with an associated time step  $\Delta t$  and trajectory length  $K\Delta t = \Delta\mathcal{T}$ .

*Initial distribution for the cloning algorithm.* To begin, we identify the cell in which the trajectory starts, i.e., we determine the indices  $(i_0, j_0)$  such that  $\varphi(0) \in S_{i_0, j_0}$ . We then randomly choose  $M_0$  of the recorded trajectories from the cells  $S_{i, j}$  with  $i \in \{i_0 - 2, i_0 - 1, \dots, i_0 + 2\}$ ,  $j \in \{j_0 - 2, j_0 - 1, \dots, j_0 + 2\}$ ; the trajectories are chosen from a uniform distribution on all the trajectories that start within these cells and with replacement. This initial condition models a smeared-out delta peak at the initial tube center  $\varphi(0)$ .

*Iteration step of the cloning algorithm.* To infer the decay of the sojourn probability until the final time  $t_f$ , the iteration step described in the following is repeated  $\mathcal{N} = t_f/\Delta\mathcal{T}$  times. In the  $l$ th repetition, the sojourn probability is obtained for  $t \in [l\Delta\mathcal{T}, (l+1)\Delta\mathcal{T}]$ . For  $l = 0$ ,  $M_0$  sample time series have been selected as described above; for  $l \geq 1$ ,  $M_l$  sample time series have been selected as will be described further below.

In the  $l$ th iteration step, we follow the  $M_l$  sample time series for the duration  $\Delta\mathcal{T}$ , and keep track of how many sample time series have never left the instantaneous tube (i.e., the moving circle with radius  $R$  and center parametrized by  $\varphi$ ) between the initial time of the  $l$ th iteration,  $t_{l,0} \equiv l\Delta\mathcal{T}$ , and each later instant  $t_{l,k} \equiv l\Delta\mathcal{T} + k\Delta t$ , where  $0 \leq k \leq K$ . We denote by  $M_{l,k}$  the number of trajectories that have never left the tube until time  $t_{l,k}$ , so that  $M_{l,0} \equiv M_l$ . For the time interval  $[l\Delta\mathcal{T}, (l+1)\Delta\mathcal{T}]$ , we then approximate the sojourn probability as

$$P_R^\varphi(t_{l,k}) = \left( \prod_{m=0}^{l-1} \frac{M_{m,K}}{M_m} \right) \frac{M_{l,k}}{M_l}, \quad 0 \leq k \leq K, \quad (\text{B1})$$

where for  $l = 0$  the product is defined as 1 (the product describes the overall decay of the sojourn probability until time  $l\Delta\mathcal{T}$ , i.e., the sojourn probability until the beginning of the current time interval  $[l\Delta\mathcal{T}, (l+1)\Delta\mathcal{T}]$ ).

From the  $M_{l,K}$  sample trajectories that have remained within the tube until time  $t_{l,K} \equiv l\Delta\mathcal{T} + K\Delta t = (l+1)\Delta\mathcal{T}$ , we construct a normalized histogram using the bins  $S_{ij}$  defined in Eq. (A1). Using this histogram as probability distribution on the cells  $S_{ij}$ , and employing a uniform distribution for the recorded time series within each cell  $S_{ij}$ , we draw  $M_{l+1}$  new time series from the data set from Appendix A. In the  $(l+1)$ -th iteration of the algorithm, we then follow these newly drawn trajectories.

All trajectories in the algorithm are drawn with replacement; if the initial position of a drawn trajectory is not within the tube initially (which can occur if a cell only partly overlaps

with the instantaneous tube), a new trajectory is drawn from the same cell  $S_{ij}$  until the initial condition of the sample is within the instantaneous tube. As detailed at the end of the present Appendix, we choose the values of  $M_l$  dynamically, depending on the current trend of the sojourn probability.

*Numerical calculation of exit rate from sojourn probability.* The decay of the sojourn probability is quantified by the instantaneous exit rate at which trajectories first leave the tube, as defined in Eq. (2). To calculate the exit rate numerically, we discretize Eq. (2) using the central difference scheme with the same time step  $\Delta t$  as used for the sample data. We then evaluate the time-discretized expression using the measured sojourn probability (B1).

*Estimating the number of samples.* The algorithm we use to measure sojourn probabilities from simulations relies on repeated random sampling of recorded time series. To choose the number of drawn samples  $M_l$  efficiently, we employ the same algorithm as used in Ref. [22]. More explicitly, at the beginning of the  $l$ th repetition ( $l > 1$ ) of the cloning algorithm, we fit a linear function

$$\alpha_{\text{fit}}(t) = a(t - l\Delta\mathcal{T}) + b, \quad (\text{B2})$$

to the measured exit rate in the time interval  $[l\Delta\mathcal{T} - \Delta t_{\text{fit}}, l\Delta\mathcal{T}]$ , where  $\Delta t_{\text{fit}}/\tau_D = \min\{0.05, \Delta\mathcal{T}/\tau_D\}$ . This fit quantifies the trend of the sojourn probability in the recent past. We use the fitted exit rate to estimate the expected decay of the sojourn probability for the next iteration duration  $\Delta\mathcal{T}$ , and choose  $M_l$  such that at the end of the iteration step we expect to have  $N_{\text{final}}$  trajectories remaining inside the tube. This leads to

$$N_{\text{final}} = M_l \exp \left[ - \int_{l\Delta\mathcal{T}}^{(l+1)\Delta\mathcal{T}} \alpha_{\text{fit}}(s) ds \right], \quad (\text{B3})$$

$$\iff M_l = N_{\text{final}} \exp \left[ a \frac{\Delta\mathcal{T}^2}{2} + b \Delta\mathcal{T} \right]. \quad (\text{B4})$$

Unless noted otherwise, we use  $M_0 = 5 \times 10^4$  and  $N_{\text{final}} = 2 \times 10^4$  for all data shown in the present work.

### APPENDIX C: SOJOURN-PROBABILITY MCMC ALGORITHM FOR MEDIUM ENTROPY PRODUCTION

We now summarize the Metropolis-Hastings algorithm [23], which we use for our Markov chain Monte Carlo (MCMC) sampling of the transition path ensemble. We approximate the space of transition paths from  $\mathbf{x}_0 = (0, 0)$  to  $\mathbf{x}_f = (L, L)$  by Eq. (13). We consider  $M = 15$  two-dimensional mode vectors, so that we run the MCMC algorithm on a space of dimension  $d = 30$ .

*Initialization.* As initial condition for the MCMC algorithm, we draw a random state  $\mathbf{a}^{(0)} = \kappa \boldsymbol{\eta}$ , with  $\boldsymbol{\eta}$  a sample from a  $d$ -dimensional normal distribution with vanishing mean and unit covariance matrix, and  $\kappa = 1/10$  a scaling factor that determines the covariance of the initial state  $\mathbf{a}^{(0)}$ ; we comment on our choice for  $\kappa$  at the end of the present Appendix.

*Monte Carlo step.* In the  $k$ th MCMC step, a candidate  $\mathbf{a}'$  for the subsequent state  $\mathbf{a}^{(k+1)}$  is proposed from the current state  $\mathbf{a}^{(k)}$  via  $\mathbf{a}' = \mathbf{a}^{(k)} + \kappa \boldsymbol{\eta}$ , where  $\boldsymbol{\eta}$  is drawn from a  $d$ -dimensional normal distribution with vanishing mean and

unit covariance matrix, and we use the same scaling factor  $\kappa = 1/10$  as for the initialization. We subsequently evaluate the log ratio of path probabilities for the paths corresponding to  $\mathbf{a}'$ ,  $\mathbf{a}^{(k)}$ ,

$$\xi \equiv \ln \frac{P(\mathbf{a}')}{P(\mathbf{a}^{(k)})} \equiv \lim_{R \rightarrow 0} \ln \frac{P_R^{\phi(\mathbf{a}')}}{P_R^{\phi(\mathbf{a}^{(k)})}}, \quad (\text{C1})$$

by extrapolating the log ratio of measured finite-radius sojourn probabilities to the limit  $R = 0$  [22]. More explicitly, for the paths corresponding to  $\mathbf{a}'$ ,  $\mathbf{a}^{(k)}$ , we use the cloning algorithm from Appendix B to measure the finite-radius sojourn probabilities for tube radius  $R/L = 0.3, 0.5, 0.7$ . This yields three data points for the finite-radius log ratio  $\ln P_R^{\phi(\mathbf{a}')}/P_R^{\phi(\mathbf{a}^{(k)})}$ , which we extrapolate to zero by fitting  $f(R) = a + R^2 b$  and using  $\lim_{R \rightarrow 0} \ln P_R^{\phi(\mathbf{a}')}/P_R^{\phi(\mathbf{a}^{(k)})} \equiv a$  [22]. To determine whether the proposed state  $\mathbf{a}'$  is accepted, we draw a random number  $u$  from a uniform distribution on  $[0, 1]$ . If  $u \leq e^\xi \equiv P(\mathbf{a}')/P(\mathbf{a}^{(k)})$ , we set  $\mathbf{a}^{(k+1)} = \mathbf{a}'$  as the next MCMC state; otherwise we use  $\mathbf{a}^{(k+1)} = \mathbf{a}^{(k)}$  [23].

*Evaluation of medium entropy production.* The MCMC algorithm yields a sequence of transition paths parametrized by their expansion coefficients, i.e.,  $(\mathbf{a}^{(0)}, \mathbf{a}^{(1)}, \dots)$ . For every fifth path we evaluate the medium entropy production via Eq. (1). Since the forward path sojourn probabilities for radius  $R/L = 0.3, 0.5, 0.7$  have already been measured for the MCMC step, we only need to evaluate the corresponding backward path sojourn probabilities to obtain the entropy production along the path. For every fifth path we therefore measure the backward-path sojourn probabilities at radius  $R/L = 0.3, 0.5, 0.7$ , then fit a quadratic function  $f(R) = a + R^2 b$  to the log ratio  $\ln P_R^{\phi(\mathbf{a}^{(k)})}(t_f)/P_R^{\tilde{\phi}(\mathbf{a}^{(k)})}(t_f)$ , and extrapolate to  $R \rightarrow 0$  as  $\lim_{R \rightarrow 0} \ln P_R^{\phi(\mathbf{a}^{(k)})}(t_f)/P_R^{\tilde{\phi}(\mathbf{a}^{(k)})}(t_f) \equiv a$ .

*Numerical parameters for sojourn probabilities.* For the evaluation of all finite-radius sojourn probabilities in the MCMC algorithm we use the time series from Appendix A with  $\theta = 1$ , and the algorithm from Appendix B with  $M_0 = 10^4$  and  $N_{\text{final}} = 5 \times 10^3$ .

To decrease the influence of initial conditions in the measurement of the sojourn probability, as observed at the far ends of Fig. 2(c), we do not use the delta-peak initial conditions described in Appendix B. Instead, before starting the MCMC algorithm, we for each radius  $R/L = 0.3, 0.5, 0.7$ , and each of the points  $\mathbf{x}_0, \mathbf{x}_f$ , consider a constant path; i.e., we consider circles of radius  $R$  around both the initial and final points. We use the algorithm from Appendix B to let the delta-peak initial condition relax to the respective steady-state absorbing-boundary decay on those circles around  $\mathbf{x}_0, \mathbf{x}_f$ . We then use the corresponding normalized spatial distributions as initial conditions for each evaluation of the forward (backward) sojourn probability in the MCMC algorithm.

To increase the number of samples, and to decrease correlations among the samples, we run 90 independent MCMC algorithms in parallel. We discard the first 1000 steps of each MCMC run to account for the fact that the initial condition  $\mathbf{a}^{(0)}$  might correspond to a very atypical transition path. After subtracting the first 1000 steps, the MCMC data comprise 287 240 MCMC steps (the number of steps in the individual MCMC runs ranges, after subtracting the first 1000 steps,

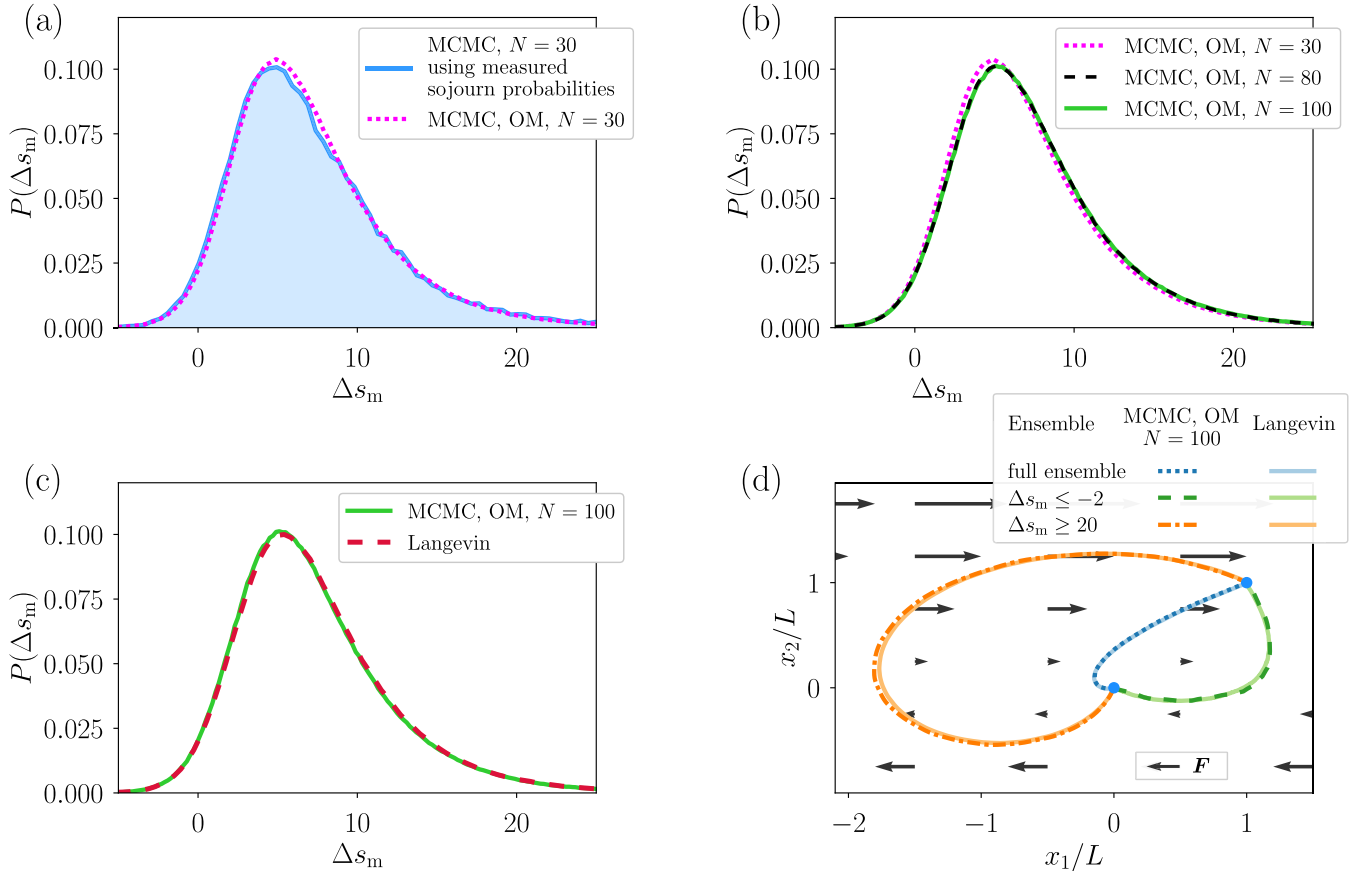


FIG. 4. (a) The solid blue line is a replot of the medium-entropy-production distribution shown in Fig. 3(a), which is inferred using an MCMC algorithm that uses measured sojourn probabilities; cf. Appendix C. The dotted magenta line displays the medium-entropy-production distribution obtained from using the same MCMC algorithm, but evaluating ratios of path probabilities and the medium entropy production using analytical expressions; cf. Appendix D. Consequently, the “OM” in the legend refers to the Onsager-Machlup action (7). Both algorithms use the path-space parametrization (13) with  $M = 15$ . (b) The distribution of the medium entropy production for the ensemble of paths that start at  $\mathbf{x}_0 = (0, 0)$  and at time  $t = \tau_D$  are at  $\mathbf{x}_f = (L, L)$ . Distributions are obtained using the theoretical MCMC algorithm from Appendix D, with  $M = 15$  [dotted magenta line, replot from panel (a)],  $M = 40$  (dashed black line), and  $M = 50$  (solid green line). (c) The solid green line is a replot of the  $M = 50$  data from panel (c). The dashed red line is a replot of the corresponding data from Fig. 3(a) and shows the medium entropy production for the ensemble of paths that start at  $\mathbf{x}_0 = (0, 0)$  and at time  $t = \tau_D$  are at  $\mathbf{x}_f = (L, L)$ , obtained from evaluating the formula (9) on trajectories generated from direct Langevin simulations. (d) The solid colored lines are replots of the corresponding data in Fig. 3(b). The blue dotted and solid curves represent the mean path for the full ensemble of paths that move from  $\mathbf{x}_0 = (0, 0)$  to  $\mathbf{x}_f = (1, 1)$  in a time  $t = \tau_D$ . While the dash-dotted and solid orange lines show the mean over such paths with entropy production  $\Delta s_m \geq 20$ , the dashed and solid green lines denote the mean for low-entropy production paths with  $\Delta s_m \leq -2$ . All solid lines are obtained from direct Langevin simulation, the corresponding broken lines represent means for the  $N = 100$  theoretical MCMC data; cf. panels (b) and (c).

from 1245 to 6295). Since we use only every fifth MCMC step to calculate a sample for the medium entropy production, our MCMC data in total yield  $287\,240/5 = 57\,448$  samples for  $\Delta s_m$ .

We now briefly discuss our choice of the step size parameter  $\kappa$ . Preliminary MCMC runs showed that, for our model system and parameters, in the subdomain of  $\mathbb{R}^d$  for which  $P(\mathbf{a})$  and the product  $\Delta s_m P(\mathbf{a})$  are non-negligible, the components of the vector  $\mathbf{a} \in \mathbb{R}^d$  are of order 1. This means that if a typical MCMC step changes any component of the vector  $\mathbf{a}$  by a number much larger than 1, the algorithm will frequently try to leave the relevant subdomain of  $\mathbb{R}^d$  within a single step, which leads to a low MCMC acceptance rate, and hence a large number of MCMC steps necessary to explore the relevant domain. On the other hand, if a typical MCMC step changes the components of the vector  $\mathbf{a}$  by only a number

much smaller than 1, it will take many steps to explore the relevant domain.

The above heuristic arguments motivate our choice  $\kappa = 1/10$  for the MCMC step: The factor  $1/10$  means that in each MCMC step we attempt to vary each vector component of  $\mathbf{a}$  on a scale one order of magnitude smaller as compared to the relevant subdomain. Ultimately, the justification for our choice of  $\kappa$  is that our MCMC data are reasonably converged, as discussed in Appendix D and in particular in Fig. 4(a) below.

We have chosen  $\kappa = 1/10$  also in our initial condition so as to be consistent with our MCMC step. Note that, since we disregard the first 1000 steps of each MCMC run, the details of the initial condition are in fact not important for our result, as long as the initial values for each component of  $\mathbf{a}^{(0)}$  are of the order of unity.



#### APPENDIX D: FURTHER ANALYSIS OF THE DEVIATION BETWEEN THE ENTROPY DISTRIBUTIONS OBTAINED FROM SOJOURN-PROBABILITY MCMC AND DIRECT LANGEVIN SIMULATIONS

In Fig. 3(a) we consider the distribution of the medium entropy production, obtained (1) from the sojourn-probability MCMC algorithm described in Appendix C and (2) from the theoretical formula, Eq. (9), evaluated on directly simulated Langevin trajectories. In the present Appendix, we demonstrate that the slight differences in the two data sets can be explained by the number of modes used in the parametrization (13), which, for the MCMC data shown in Fig. 3, is  $M = 15$ .

For this, we consider a variation of the MCMC algorithm described in Appendix C. In this variation, we do not use recorded sample trajectories to evaluate ratios of path probabilities and the entropy production, but instead use (1) the difference in Onsager-Machlup actions (7) for log ratios of path probabilities and (2) the analytical formula, Eq. (9), for the medium entropy production. To distinguish it from the data-driven MCMC algorithm described in Appendix C, we in the following refer to this MCMC algorithm as “theoretical MCMC”; here “theoretical” means that neither path probabilities nor entropy productions are measured from data, but rather evaluated using the corresponding analytical formulas available for overdamped Langevin dynamics. We run the theoretical MCMC using the same parameters for the cloning algorithm as in Appendix C. For each parameter combination considered below, we run 100 independent theoretical MCMC realizations with 200 000 steps each, and evaluate the medium entropy production for every MCMC step. We discard the first 999 MCMC steps for each run, which means that for each parameter combination, our theoretical MCMC ensemble consists of in total  $100 \times (199\,001) \approx 1.99 \times 10^7$  data points for  $\Delta s_m$ . Thus, for the theoretical MCMC we have two orders of magnitude more MCMC paths as compared to the data-driven MCMC results shown in Fig. 3, which is because the theoretical MCMC is computationally much cheaper.

We now show that the deviations between the two curves in Fig. 3(a) originate from the relatively low number of modes we use,  $M = 15$ . For this, we consider the theoretical MCMC with also  $M = 15$  modes, i.e., the same number of modes as used for the sojourn-probability MCMC in Fig. 3(a). We compare the sojourn-probability and theoretical-MCMC results in Fig. 4(a), where we observe that the distributions are very similar, with only minor deviations around  $\Delta s_m \approx 5$ . This indicates that the sojourn-probability MCMC data are sufficiently converged, and that the deviations from the direct Langevin simulations are due to the low-dimensional approximation  $M = 15$  of the path space. We chose  $M = 15$  in the main text as a compromise between approximation error (which decreases with increasing  $M$ ) and convergence speed of the MCMC algorithm (which decreases with increasing  $M$ ).

We additionally run the theoretical MCMC algorithm for  $M = 40$  and  $M = 50$  mode vectors, corresponding to  $N = Md = 80, 100$ , respectively. The resulting distributions are shown in Fig. 4(b), where we observe that the  $M = 15$  data slightly disagree with the  $M = 40, 50$  results. This confirms that the projection on only  $M = 15$  modes leads to a distortion

of the actual distribution of the medium entropy production. The distributions for  $M = 40$  and  $M = 50$  modes agree with each other very well, so that we conclude that  $M \geq 40$  modes are enough to reproduce the actual distribution. Indeed, the  $M = 50$  theoretical MCMC data agree very well with the direct Langevin results; see Fig. 4(c).

In Fig. 4(d) we finally compare the mean paths obtained from direct Langevin simulations, shown in Fig. 3(b), to the corresponding mean paths of the  $M = 50$  theoretical MCMC data. We observe that all three path pairs are in very good agreement; this once again confirms the validity of the MCMC algorithm.

#### APPENDIX E: ENTROPY PRODUCTION ALONG CLOSED LOOPS IN A CIRCULAR DOUBLE WELL

We here consider a second example system. For a length scale  $L$  and a timescale  $\tau$ , we again consider the overdamped Itô-Langevin Eq. (5) for dimension  $N = 2$  with diffusivity  $D = L^2/T$ , so that  $\tau_D \equiv L^2/D = \tau$ . We now consider a force  $F$ ,

$$F(\mathbf{x}) = -(\nabla U)(\mathbf{x}) + \theta F_{\text{neq}}(\mathbf{x}), \quad (\text{E1})$$

which is given as a sum of the gradient of a potential  $U$  and an additional term  $F_{\text{neq}}$  which is nonconservative, i.e., does not admit a (global) potential. As in the main text, the dimensionless parameter  $\theta \in \mathbb{R}$  controls the amplitude of the nonconservative force, and for  $\theta \neq 0$  this system is a nonequilibrium system. For  $U$  we consider a sombrero potential superimposed with an angular double well, defined as

$$U(\mathbf{x}) = U_0 \left[ \left( \frac{\|\mathbf{x}\|}{L} \right)^2 - 1 \right]^2 + U_1 \left[ \frac{1 + \cos(2\phi)}{2} \frac{1 + \exp\left(\frac{1}{10}\right)}{1 + \exp\left(\frac{\|\mathbf{x}\|^2}{10L^2}\right)} - 1 \right], \quad (\text{E2})$$

where  $\|\mathbf{x}\| = \sqrt{x_1^2 + x_2^2}$ ,  $x_1 = \|\mathbf{x}\| \cos(\phi)$ ,  $x_2 = \|\mathbf{x}\| \sin(\phi)$ ; we use  $\beta U_0 = 5$ ,  $\beta U_1 = 2$ . This potential, which is illustrated in Fig. 5(a), has local minima at  $\mathbf{x} = (L, 0)$ ,  $(-L, 0)$  and saddle points at  $\mathbf{x} = (0, L)$ ,  $(0, -L)$ . For the nonequilibrium force we consider an angular force

$$\frac{1}{T} F_{\text{neq}}(\mathbf{x}) = \frac{1}{\|\mathbf{x}\|^2} \begin{pmatrix} -x_2 \\ x_1 \end{pmatrix}, \quad (\text{E3})$$

which is illustrated as a quiver plot in Fig. 5(a).

For the force (E1), (E2), and (E3) and  $\varphi$  a closed loop, the analytical entropy production (10) is given by

$$\Delta s_m[\varphi] = 2\pi\Gamma\theta, \quad (\text{E4})$$

where  $\Gamma \in \mathbb{Z}$  is the winding number which quantifies how often the path  $\varphi$  winds counterclockwise around the origin  $\mathbf{x} = \mathbf{0}$ . Thus, for the particular nonequilibrium force (E3), the theoretical entropy production (E4) is topological, i.e., depends on only the winding number and not on more details of the path.

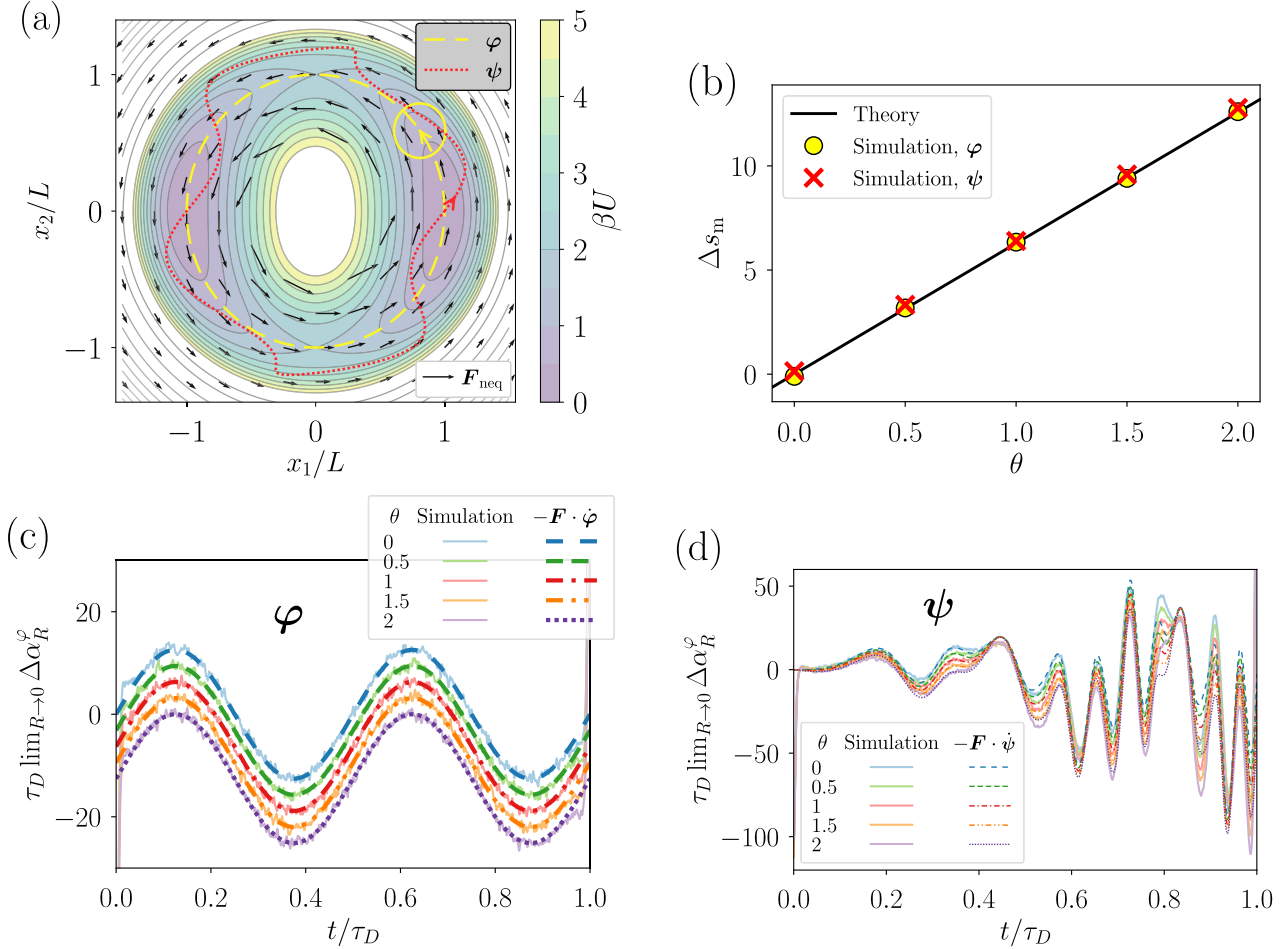


FIG. 5. (a) The colored contours show the potential  $U$  defined in Eq. (E2). The nonequilibrium force Eq. (E3) is shown as black quiver plot. The dashed yellow line denotes the path  $\varphi$  defined in Eq. (E5), and the yellow circle indicates an instantaneous ball of radius  $R/L = 0.2$  around  $\varphi$ . The dotted red line denotes the path  $\psi$  defined in Eq. (E6). For both paths  $\varphi, \psi$ , arrows indicate the forward direction. (b) The black line denotes the theoretical entropy production (E4) for  $\Gamma = 1$ . The colored symbols denote the entropy production obtained by evaluating the right-hand side of Eq. (1) using extrapolated measured sojourn probabilities. The dots correspond to  $\varphi$ ; the crosses are obtained using  $\psi$ . (c, d) The solid colored lines denote the extrapolation to  $R \rightarrow 0$  of measured finite-radius exit-rate differences between forward and backward paths, for several values of  $\theta$  and the reference path (c)  $\varphi$  and (d)  $\psi$ . The broken colored lines denote the corresponding theoretical predictions given by the right-hand side of Eq. (9), calculated using the force (E1). Numerical data are smoothed using a Hann window of width  $0.005 \tau_D$ .

We consider two circular paths

$$\varphi_t = L \begin{pmatrix} \cos(2\pi t/t_f) \\ \sin(2\pi t/t_f) \end{pmatrix}, \quad (\text{E5})$$

$$\psi_t = L \begin{pmatrix} \cos(2\pi t^2/t_f^2) \\ \sin(2\pi t^2/t_f^2) \end{pmatrix} + \frac{L}{5} \begin{pmatrix} \sin(10\pi t^2/t_f^2) \\ \sin(2\pi t^2/t_f^2) \end{pmatrix}, \quad (\text{E6})$$

where  $t \in [0, t_f] \equiv [0, \tau]$ . These paths, which both have a winding number  $\Gamma = 1$ , are shown in Fig. 5(a) as yellow dashed and dotted red lines.

For  $\theta = 0, 0.5, 1, 1.5, 2$  and  $R/L = 0.2, 0.25, 0.3, 0.35, 0.4, 0.45, 0.5$ , we measure the entropy production along the forward and reverse version of each path  $\varphi, \psi$ , using a variation of the cloning algorithm from Appendix B: Instead of binning space, and creating a set of sample time series beforehand, we run simulations on the fly. Initial conditions for the  $(n+1)$ -th iteration are then sampled from a uniform distribution on the final positions of the trajectories that have

never left the tube in the  $n$ th iteration. Also here simulations are run using the standard Euler-Maruyama, but since we now consider smaller tube radii, we also use a smaller time step  $\Delta t/\tau_D = 10^{-5}$  as well as shorter iteration times  $\Delta \mathcal{T}/\tau_D = 0.005$ . We furthermore use  $M_0 = N_{\text{final}} = 10^5$  and a delta-peak initial condition at the initial tube center.

We extrapolate the resulting measured finite-radius exit-rate differences between forward and reverse paths  $R = 0$  as described in the main text, and in Figs. 5(c) and 5(d) we show that the result agrees well with the theoretical prediction (9) along the paths. Finally, in Fig. 5(b) we compare the negative temporal integral of the extrapolated exit-rate differences with the expected theoretical entropy production, and find that the numerical and theoretical results agree very well. Thus, also this second example confirms that Eqs. (1) and (3) can be used to infer and analyze the medium entropy production along individual paths directly from exit rates.

- [1] S. Chandrasekhar, *Rev. Mod. Phys.* **15**, 1 (1943).
- [2] A. Kolmogoroff, *Math. Ann.* **113**, 766 (1937).
- [3] A. M. Yaglom, *Mat. Sb. (N.S.)* **24**, 457 (1949).
- [4] N. Ikeda and S. Watanabe, *Stochastic Differential Equations and Diffusion Processes*, 2nd ed., North-Holland Mathematical Library (North-Holland, Amsterdam, 1989), Vol. 24.
- [5] C. Maes and K. Netočný, *J. Stat. Phys.* **110**, 269 (2003).
- [6] U. Seifert, *Phys. Rev. Lett.* **95**, 040602 (2005).
- [7] G. N. Bochkov and E. Kuzovlev, *Sov. Phys. JETP* **45**, 125 (1977).
- [8] C. Jarzynski, *Phys. Rev. Lett.* **78**, 2690 (1997).
- [9] J. Kurchan, *J. Phys. A: Math. Gen.* **31**, 3719 (1998).
- [10] G. E. Crooks, *Phys. Rev. E* **60**, 2721 (1999).
- [11] C. Maes, in *Poincaré Seminar 2003*, edited by J. Dalibard, B. Duplantier, and V. Rivasseau (Birkhäuser, Basel, 2004), pp. 145–191.
- [12] V. Y. Chernyak, M. Chertkov, and C. Jarzynski, *J. Stat. Mech.: Theory Exp.* (2006) P08001.
- [13] U. Seifert, *Rep. Prog. Phys.* **75**, 126001 (2012).
- [14] K. Sekimoto, *Stochastic Energetics*, Lecture Notes in Physics (Springer, Heidelberg, 2010), Vol. 799.
- [15] U. Seifert, *Annu. Rev. Condens. Matter Phys.* **10**, 171 (2019).
- [16] D. G. Luchinsky and P. V. E. McClintock, *Nature (London)* **389**, 463 (1997).
- [17] D. G. Luchinsky, P. V. E. McClintock, and M. I. Dykman, *Rep. Prog. Phys.* **61**, 889 (1998).
- [18] S. Otsubo, S. Ito, A. Dechant, and T. Sagawa, *Phys. Rev. E* **101**, 062106 (2020).
- [19] S. K. Manikandan, D. Gupta, and S. Krishnamurthy, *Phys. Rev. Lett.* **124**, 120603 (2020).
- [20] C. Tietz, S. Schuler, T. Speck, U. Seifert, and J. Wrachtrup, *Phys. Rev. Lett.* **97**, 050602 (2006).
- [21] J. Kappler and R. Adhikari, *Phys. Rev. Research* **2**, 023407 (2020).
- [22] J. Gladrow, U. F. Keyser, R. Adhikari, and J. Kappler, *Phys. Rev. X* **11**, 031022 (2021).
- [23] J. Thijssen, *Computational Physics*, 2nd ed. (Cambridge University Press, Cambridge, 2007).
- [24] A. Ben-Naim, *A Farewell to Entropy: Statistical Thermodynamics Based on Information* (World Scientific, Singapore, 2008).
- [25] H. Ito, *Prog. Theor. Phys.* **59**, 725 (1978).
- [26] T. Fujita and S.-i. Kotani, *J. Math. Kyoto Univ.* **22**, 115 (1982).
- [27] L. Onsager and S. Machlup, *Phys. Rev.* **91**, 1505 (1953).
- [28] D. Dürr and A. Bach, *Commun. Math. Phys.* **60**, 153 (1978).
- [29] Y. Takahashi and S. Watanabe, in *Stochastic Integrals*, edited by D. Williams Lecture Notes in Mathematics (Springer, Berlin, 1981), Vol. 851, pp. 433–463.
- [30] S. Bo, S. H. Lim, and R. Eichhorn, *J. Stat. Mech.: Theory Exp.* (2019) 084005.
- [31] N. G. van Kampen, *J. Stat. Phys.* **24**, 175 (1981).
- [32] N. G. v. Kampen, *Stochastic Processes in Physics and Chemistry*, 3rd ed., North-Holland Personal Library (Elsevier, Amsterdam, 2007).
- [33] C. W. Gardiner, *Stochastic Methods: A Handbook for the Natural and Social Sciences*, 4th ed., Springer Series in Synergetics (Springer, Berlin, 2009).
- [34] M. E. Cates, [arXiv:1904.01330](https://arxiv.org/abs/1904.01330) [cond-mat] (2019).